Journal of Advanced Ceramics
2020, **9**(4): 471–480
https://doi.org/10.1007/s40145-020-0390-9
ISSN 2226-4108
CN 10-1154/TQ

Research Article

Low-temperature sintering and microwave dielectric properties of $CaMg_{1-x}Li_{2x}Si_2O_6$ (x = 0–0.3) ceramics

Fangyi HUANG[a], Hua SU[a,b,*], Yuanxun LI[a,b], Huaiwu ZHANG[a], Xiaoli TANG[a]

[a]*State Key Laboratory of Electronic Thin Films and Integrated Devices, University of Electronic Science and Technology of China, Chengdu 610054, China*
[b]*Jiangxi Guo Chuang Industrial Park Development Co., Ltd., Ganzhou 341000, China*

Received: December 24, 2019; Revised: May 22, 2020; Accepted: May 22, 2020

Abstract: In this study, low-temperature fired $CaMg_{1-x}Li_{2x}Si_2O_6$ microwave dielectric ceramics were prepared via the traditional solid-state reaction method. In this process, 0.4 wt% Li_2CO_3–B_2O_3–SiO_2–$CaCO_3$–Al_2O_3 (LBSCA) glass was added as a sintering aid. The results showed that ceramics consisted of $CaMgSi_2O_6$ as the main phase. The second phases were $CaSiO_3$ always existing and Li_2SiO_3 occurring at substitution content $x > 0.05$. Li^+ substitution effectively lowered sintering temperature due to 0.4 wt% LBSCA and contributed to grain densification, and the most homogeneous morphology could be observed at $x = 0.05$. The effects of relative density, the second phase, and ionic polarizability on dielectric constant (ε_r) were investigated. The quality factor ($Q \times f$) varied with packing fraction that concerned the second phase. Moreover, the temperature coefficient of the resonant frequency (τ_f) was influenced by MgO_6 octahedral distortion and bond valence. Excellent dielectric properties of the $CaMg_{1-x}Li_{2x}Si_2O_6$ ceramic was exhibited at $x = 0.05$ with ε_r = 7.44, $Q \times f$ = 41,017 GHz (f = 15.1638 GHz), and τ_f = −59.3 ppm/℃ when sintered at 900 ℃. It had a good application prospect in the field of low-temperature co-fired ceramic (LTCC) substrate and devices.

Keywords: low permittivity; low-temperature sintering; crystal structure; microwave dielectric properties

1 Introduction

Microwave dielectric ceramics constitute key materials used in microwave band communication (mainly from 300 MHz to 300 GHz). With the rapid development of information technology, microwave dielectric ceramics with low dielectric constant (ε_r), high quality factor ($Q \times f$) value, and near-zero temperature coefficient of resonant frequency (τ_f) were extensively studied [1]. Besides, low-temperature co-fired ceramics (LTCC) technology facilitates the production and integration of miniature microwave devices. Therefore, it is widely applied in the field of wireless communications [2–7]. In order to co-fire with silver electrodes, the sintering temperature of LTCC materials should be approximately 900 ℃ or lower, but most microwave dielectric ceramic densification is achieved and good properties are obtained only during high-temperature sintering. Therefore, LTCC with low permittivity and perfect microwave dielectric properties has become a

* Corresponding author.
E-mail: uestcsh@163.com

significant research object. Typical low permittivity microwave dielectric ceramic material systems mainly include Al_2O_3, silicates, tungstate, phosphates, and garnet structure compounds. As examples, the ceramics of $ZnAl_2O_4$, Li_2TiMO_5 (M = Ge, Si), $LiYGeO_4$, $AGeO_3$ (A = Mg, Zn), Li_2AGeO_4 (A = Zn, Mg), $Ba_2MGe_2O_7$ (M = Mg, Zn), $CaAl_2O_4$, $Ba_{1-x}Sr_xZnSi_3O_8$, $BaAl_{2-2x}(ZnSi)_xSi_2O_8$, and $NaCa_4V_5O_{17}$ have been investigated in recent decades [8–17]. $CaSiO_3$, Zn_2SiO_4, and Mg_2SiO_4 are three materials mainly studied in the silicate system.

Sun *et al*. [18] studied the effect of Mg^{2+} substitution of Ca^{2+} on the microwave dielectric properties of $CaSiO_3$, after which, the ceramic acquired the dielectric properties of $CaMgSi_2O_6$ sintered at 1290 ℃: ε_r = 7.46, $Q \times f$ = 59,638 GHz, and τ_f = −46 ppm/℃. Consequently, a series of studies on $CaMgSi_2O_6$ were carried out. According to these studies, many investigations concentrated on the ion substitution for Mg ions to $CaMgSi_2O_6$ ceramics were conducted to enhance the microwave dielectric properties, indifferently to sintering temperature decrease [19,20]. Furthermore, to meet the requirements of LTCC applications, the sintering temperature of $CaMgSi_2O_6$ ceramics was reduced by adding glass or fluorides with low melting points [21–23]. However, good microwave dielectric properties were achieved in a few certain studies when the sintering temperature was reduced [24].

Li-ion substitution has been proved to be an effective method to decrease the sintering temperature of the ceramics without deterioration of properties [25–28]. Certain materials, such as Li_2WO_4 containing Li-ion, demonstrated an ultra-low sintering temperature [25–27]. Besides, Du *et al*. [28] found that $Li_{2x}Mg_{2-x}SiO_4$-3 wt% Li_2CO_3−B_2O_3−Bi_2O_3−SiO_2 (LBBS) (substitution content x = 1) ceramic (sintered at 900 ℃) exhibited good dielectric properties of ε_r = 6.1, $Q \times f$ = 44,500 GHz, and τ_f = −13 ppm/℃. The contribution of Li^+ substitution to sintering temperature could be attributed to the vacancies caused by the unequal substitution, and similar phenomena could be seen in Al^{3+} substitution for Mg^{2+} and Si^{4+} [22], and Cr^{3+} substitution for Mg^{2+} [20]. Furthermore, Li_2CO_3–B_2O_3–SiO_2–$CaCO_3$–Al_2O_3 (LBSCA) glass has been reported to effectively reduce the sintering temperature of ceramics [6,29]. In the present study, the effects of Li^+ substitution for Mg^{2+} on crystal structure and microwave dielectric properties of $CaMg_{1-x}Li_{2x}Si_2O_6$ (x = 0–0.3) ceramics, with 0.4 wt% LBSCA glass as a sintering aid, were investigated.

2 Experimental

The $CaMg_{1-x}Li_{2x}Si_2O_6$ (x = 0, 0.05, 0.1, 0.15, 0.2, 0.25, and 0.3) ceramics were synthesized via the solid-state reaction method with highly pure raw materials: $CaCO_3$ (99%, Ke-Long Co., Ltd., Chengdu, China), MgO (98%, Ke-Long Co., Ltd., Chengdu, China), Li_2CO_3 (99.9%, Aladdin, Shanghai, China), and SiO_2 (99.9%, Aladdin, Shanghai, China). Different compositions of the ceramics were weighed according to the stoichiometric formula. The mixed raw powders were milled with zirconia balls and distilled water in nylon containers for 12 h. The slurries were subsequently dried in air for 24 h and calcinated at 900 ℃ for 3 h. Following, the pre-sintered powders were re-milled with 0.4 wt% LBSCA glass for 6 h and dried for 24 h. The LBSCA glass was obtained through the quenching method. Following weighing at the molar ratio of Li_2CO_3:B_2O_3:SiO_2:$CaCO_3$:Al_2O_3=52:31.06:11.99: 2.25:2.25, the mixed analytical grade raw powder was ball-milled with ethanol for 48 h, dried at 40 ℃ or lower, and melted in alumina crucible at 1000 ℃ for 2 h. Next, the alumina crucible was instantly removed from the furnace, and the molten glass was quenched in cold distilled water [29]. The crushed glass powder was added to the pre-sintered powders. The second-milled powder with LBSCA glass was mixed with 10 wt% PVA to obtain granulations that were squashed into cylinders of 12 mm in diameter and 6 mm in thickness. Sintering of these cylinders was achieved at the temperatures of 875, 900, and 925 ℃.

In order to obtain the microwave dielectric properties of the ceramics, the network analyzer based on Hakki–Coleman resonator method was used, while the τ_f value could be calculated according to Eq. (1). The microstructure images of the polished and thermally etched surfaces were observed via scanning electron microscopy (SEM: Versa3D; FEI, USA). Moreover, the bulk density was calculated via the Archimedes principle. Regarding the crystal phase compositions of the $CaMg_{1-x}Li_{2x}Si_2O_6$ ceramics, they were identified via X-ray diffraction (XRD: MinFlex 600; Rigaku, Japan), while crystal structure refinement could be obtained via the XRD diffraction data input to Fullprof software. Refined results were applied to draw the crystal structure charts with VESTA software. The τ_f (ppm/℃) values were calculated according to the following equation:

$$\tau_f = \frac{f_T - f_0}{f_0(T - T_0)} \times 10^6 \quad (1)$$

where f_T and f_0 are the resonant frequencies at T (85 ℃) and T_0 (25 ℃), respectively.

3 Results and discussion

The phase composition was confirmed through XRD patterns, as presented in Fig. 1(a), when the $CaMg_{1-x}Li_{2x}Si_2O_6$ ceramics were sintered at 900 ℃. It could be observed that the main phase $CaMgSi_2O_6$ (PDF#11-0654) and the second phase $CaSiO_3$ (PDF#27-1064) always existed indifferently to x (0–0.3) variation. When $x \geqslant 0.1$, another second phase, Li_2SiO_3 (PDF#29-0829) appeared. The unexpected phase $CaSiO_3$ of wollastonite structure was generated through the following reaction (Eq. (2)), due to low calcination temperature (900 ℃) and the same sintering temperature. This signified that the raw materials had not completely reacted at a calcination temperature of 900 ℃. Besides, the formation of Li_2SiO_3 was due to the reaction (Eq. (3)) of SiO_2 and Li_2CO_3 within the raw powder. From these results, it could be initially determined that lower than 0.2 solid solubility of Li^+ occurred in the lattice of $CaMgSi_2O_6$ phase. The presence of three crystal phases would definitely affect the microwave dielectric properties of the ceramics. Figure 1(b) shows the amplification of diffraction peaks (–2 2 1) and (3 1 0). The diffraction peaks shifted nonlinearly with the doping amount, which had a close relationship with the unit cell parameters.

$$CaCO_3 + SiO_2 \rightarrow CaSiO_3 + CO_2\uparrow \quad (2)$$

$$Li_2CO_3 + SiO_2 \rightarrow Li_2SiO_3 + CO_2\uparrow \quad (3)$$

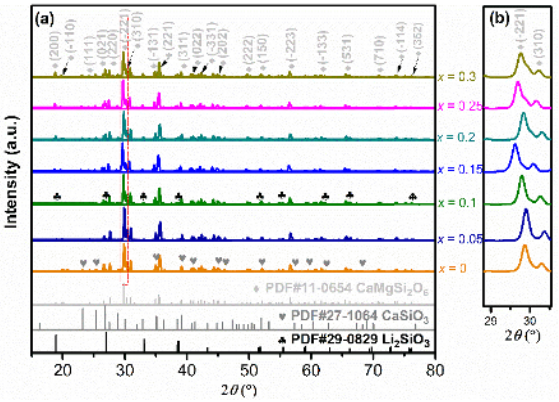

Fig. 1 (a) XRD patterns of the $CaMg_{1-x}Li_{2x}Si_2O_6$ (x = 0, 0.05, 0.1, 0.15, 0.2, 0.25, 0.3) samples sintered at 900 ℃; (b) the amplification of diffraction peaks (–2 2 1) and (3 1 0) of the $CaMgSi_2O_6$ phase.

In order to further analyze the relationship between microstructure, phase composition, and microwave dielectric properties of the ceramics, XRD data of the $CaMg_{1-x}Li_{2x}Si_2O_6$ samples sintered at 900 ℃ were refined with the Fullprof software. The theoretical models were monoclinic $CaMgSi_2O_6$ (a = 9.7397 Å, b = 8.9174 Å, and c = 5.2503 Å), triclinic $CaSiO_3$ (a = 7.9400 Å, b = 7.3200 Å, and c = 7.0700 Å), and orthorhombic Li_2SiO_3 (a = 9.3600 Å, b = 5.3950 Å, and c = 4.6750 Å). The refined plots of XRD patterns are exhibited in Figs. 2(a)–2(g) ($0 \leqslant x \leqslant 0.3$), which indicated that the calculated patterns (Y_{cal}) fitted well with the observed patterns (Y_{obs}). The reliability factors (R_p, R_{wp}, R_{exp}, and χ^2 (> 0) are the profile factor, weighted profile factor, expected weighted profile factor, and reduced chi-square, respectively) in Table 1 could also help explain that structural information, such as lattice parameters of $CaMgSi_2O_6$ phase summarized from the refinement results, was credible. Figure 3 and Table 1 demonstrate that the weight fraction of $CaSiO_3$, the lattice parameters (especially a and c), and the unit cell volume (V) shared the same trend as x increased. The fact proved that the content of Li^+ substitution, as well as the $CaSiO_3$ phase, influenced the lattice structure, which eventually affected the microwave dielectric properties. However, the diffraction peaks shifted and the unit cell volume changed inconsistently, even in the opposite trend. Besides, the refinement results of XRD data could be applied in crystal structure drawings of the three phases of the $CaMg_{1-x}Li_{2x}Si_2O_6$ ceramics with VESTA software, as presented in Figs. 4(a)–4(c). The performance of the synthesized ceramics would be affected by the three different structures synergistically and these would be discussed further. Moreover, the diffraction peak intensities (Fig. 2) and the content of $CaMgSi_2O_6$ phase (Fig. 3) demonstrated the same tendency when Li^+ substitution content increased. The microwave dielectric properties influenced by crystal structure features and the second phase could be investigated via V, bond valence, oxygen octahedron distortion calculated from bond length, and the mixture rules.

Figures 5(a)–5(g) present the morphologies of the $CaMg_{1-x}Li_{2x}Si_2O_6$ ceramic samples sintered at 900 ℃. When x = 0, the component was porous and the grain size was small, due to insufficiently high sintering temperature. Minor changes existed from Figs. 5(b) to 5(g), i.e., x value was in the interval of 0.05–0.3, considering the porosity and grain size. While when x = 0.05, the ceramic demonstrated good homogeneity in relative terms. In contrast, it was presented that the largest bulk density arises at x = 0.1 in the latter Fig. 6(b), which corresponded well with the SEM images. The enhancement of bulk density could be attributed to

Table 1 Lattice parameters and reliability factors of the $CaMg_{1-x}Li_{2x}Si_2O_6$ (x = 0, 0.05, 0.1, 0.15, 0.2, 0.25, 0.3) samples sintered at 900 ℃

x (mol)	0	0.05	0.1	0.15	0.2	0.25	0.3
a (Å)	9.74637	9.73884	9.74091	9.73582	9.74028	9.7464	9.75047
b (Å)	8.93890	8.94310	8.94625	8.94136	8.94578	8.94955	8.95045
c (Å)	5.25052	5.24970	5.25083	5.24769	5.25003	5.25222	5.25402
V (Å^3)	440.02	439.698	440.005	439.303	439.925	440.544	440.951
R_p (%)	9.00	7.86	7.97	9.01	8.19	9.37	9.44
R_{wp} (%)	10.4	8.54	8.58	10	9.04	10.5	10.6
R_{exp} (%)	9.08	8.77	9.25	8.9	9.04	8.76	9.01
χ^2	1.317	0.9481	0.8611	1.273	1.001	1.425	1.384

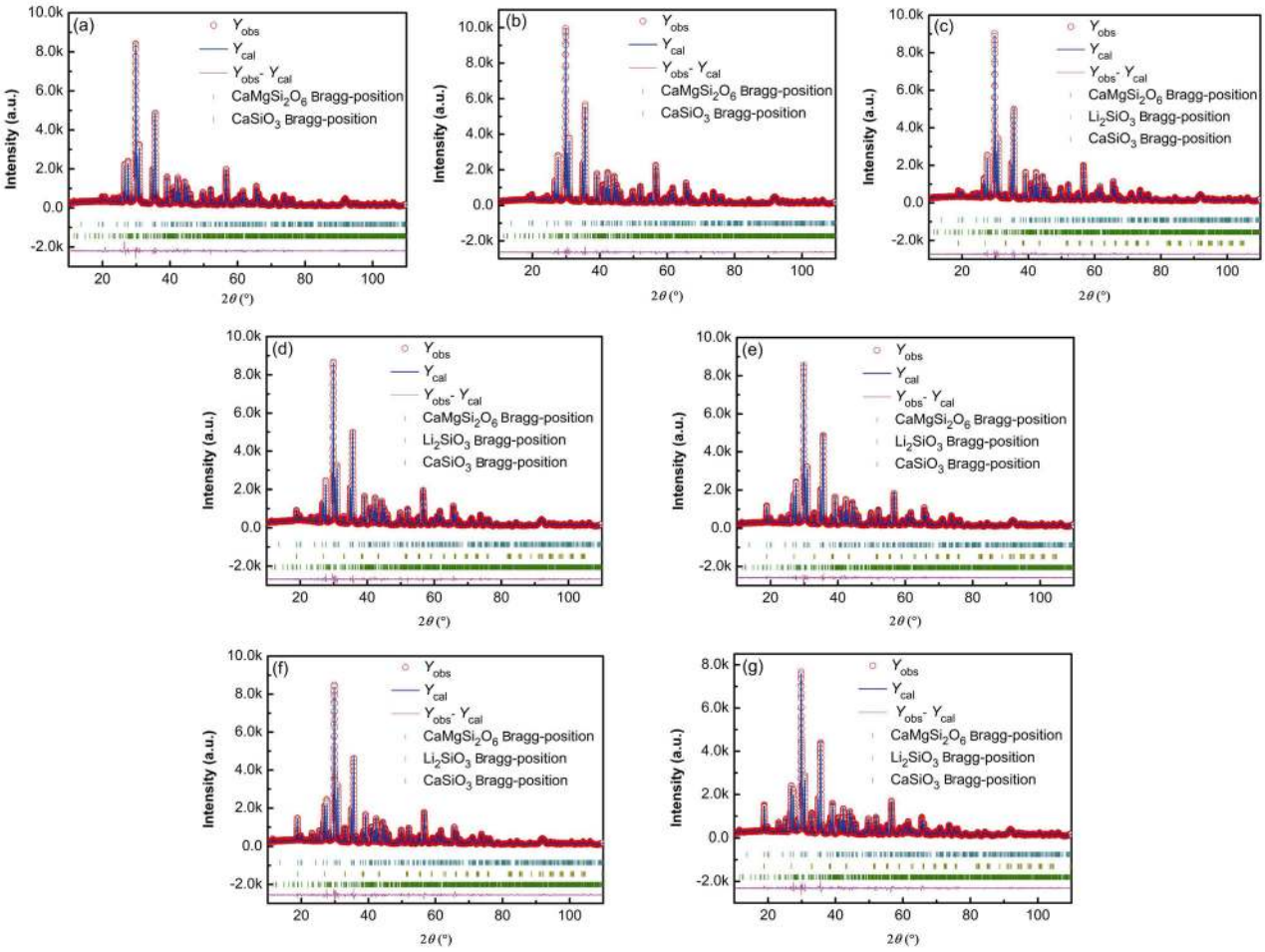

Fig. 2 Structural refinement patterns of the $CaMg_{1-x}Li_{2x}Si_2O_6$ samples sintered at 900 ℃: (a) x = 0, (b) x = 0.05, (c) x = 0.1, (d) x = 0.15, (e) x =0.2, (f) x = 0.25, and (g) x = 0.3.

O vacancies due to Eq. (4):

$$Li_2CO_3 \xrightarrow{CaMgSi_2O_6} 2Li'_{Mg} + V_O^{\cdot\cdot} + CO_2 \uparrow \quad (4)$$

The generation of vacancy defects was conducive to ion diffusion and promoted the sintering [30]. However, the grain size distribution became gradually uneven as x value increased, accompanied with the occurrence of blurred grain boundaries. This could be originated from the portion increase of the second phases and the cell volume of $CaMgSi_2O_6$ main phase. The appearance of pores might be due to the Li^+ volatilization [28]. Undoubtedly, Li^+ substitution could contribute to sintering temperature reduction and densification improvement of the $CaMg_{1-x}Li_{2x}Si_2O_6$ ceramics, which would lead to significant influences on microwave dielectric properties.

The $Q \times f$ values of the samples are presented in Fig. 7(a). Regardless of sintering temperatures, $Q \times f$

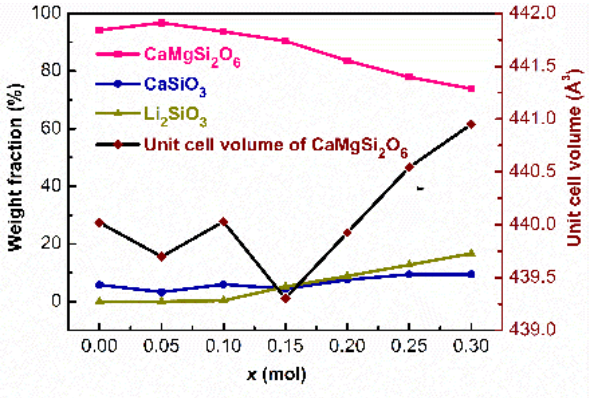

Fig. 3 Weight fraction of different phases and the unit cell volume of $CaMgSi_2O_6$ phase of the $CaMg_{1-x}Li_{2x}Si_2O_6$ (x = 0, 0.05, 0.1, 0.15, 0.2, 0.25, 0.3) ceramics sintered at 900 ℃.

values reached the optimal values at x = 0.05, where the main phases occupied the dominant positions. As known, the quality factor is primarily determined by the structure and composition of the ceramic material itself. The loss due to crystal structure characteristics constitutes an intrinsic loss, while the losses caused by non-integrity, such as the second phase, impurities, pores, cracks, and grain boundaries are called extrinsic losses [31]. In this study, no pure $CaMgSi_2O_6$ phase existed in the samples, and the highest weight fraction (Fig. 3) and peak intensity (Fig. 2) of $CaMgSi_2O_6$ were reached at x = 0.05. Consequently, the $Q \times f$ value was severely affected by both the second phase and the crystallinity simultaneously. Moreover, the packing fraction is an

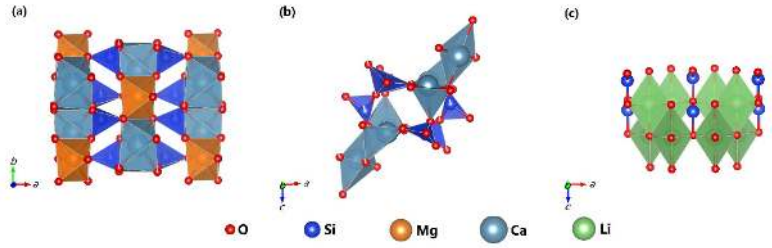

Fig. 4 Schematic of different phases in the $CaMg_{1-x}Li_{2x}Si_2O_6$ ceramics: (a) monoclinic $CaMgSi_2O_6$, (b) triclinic $CaSiO_3$, and (c) orthorhombic Li_2SiO_3.

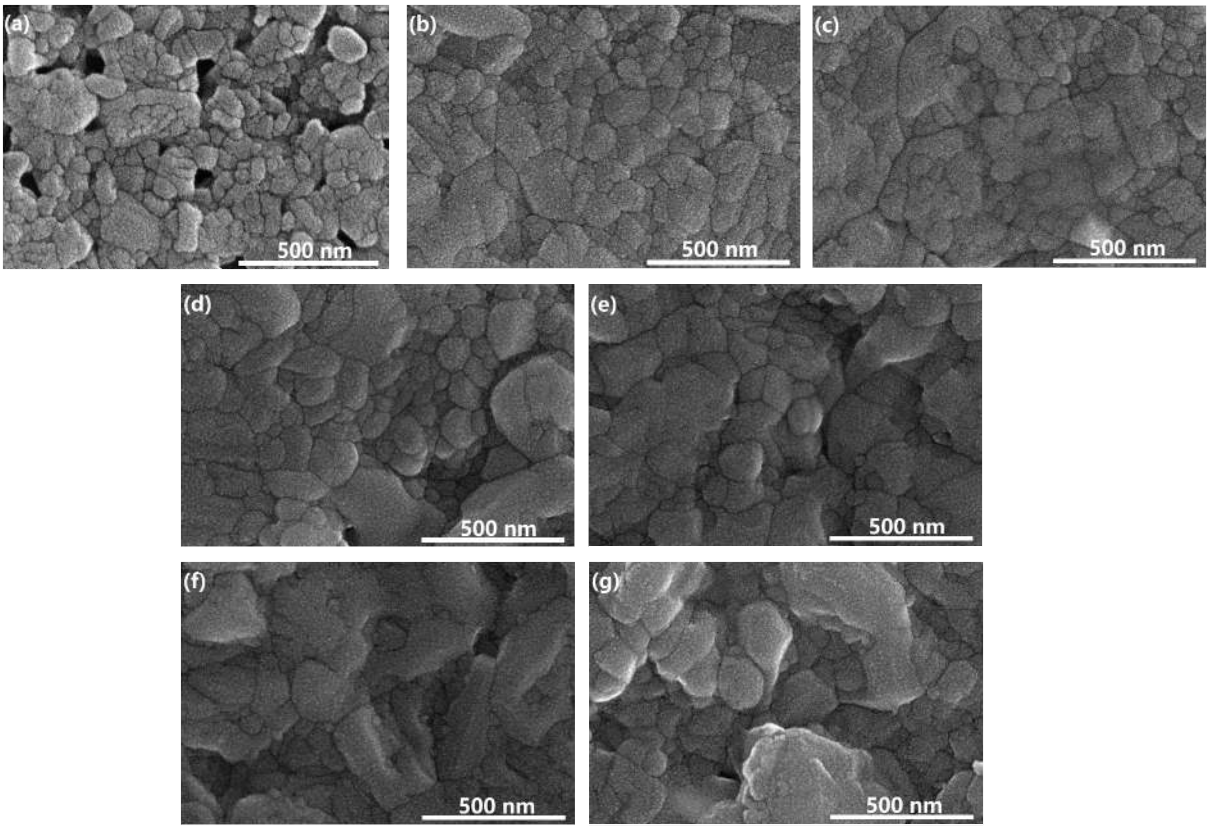

Fig. 5 SEM morphologies of the $CaMg_{1-x}Li_{2x}Si_2O_6$ samples sintered at 900 ℃: (a) x = 0, (b) x = 0.05, (c) x = 0.1, (d) x = 0.15, (e) x = 0.2, (f) x = 0.25, and (g) x = 0.3.

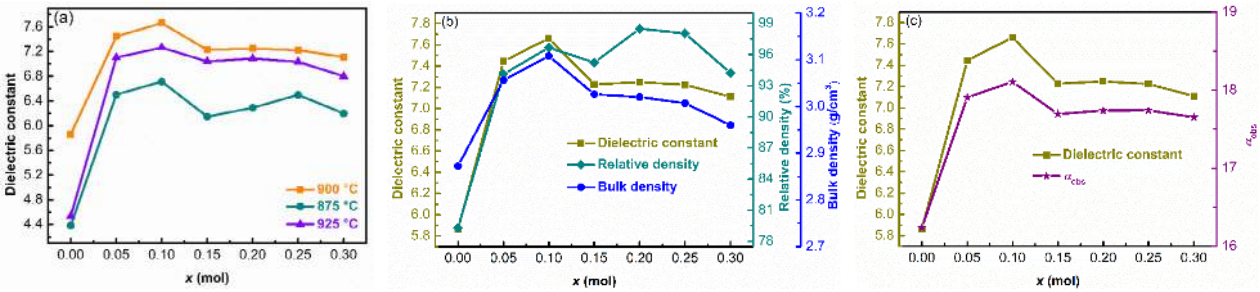

Fig. 6 (a) Dielectric constant of the $CaMg_{1-x}Li_{2x}Si_2O_6$ (x = 0, 0.05, 0.1, 0.15, 0.2, 0.25, 0.3) samples sintered under different temperatures; (b) the dielectric constant, bulk density, and relative density, and (c) the dielectric constant and observed ionic polarizability of the $CaMg_{1-x}Li_{2x}Si_2O_6$ (x = 0, 0.05, 0.1, 0.15, 0.2, 0.25, 0.3) samples sintered at 900 ℃.

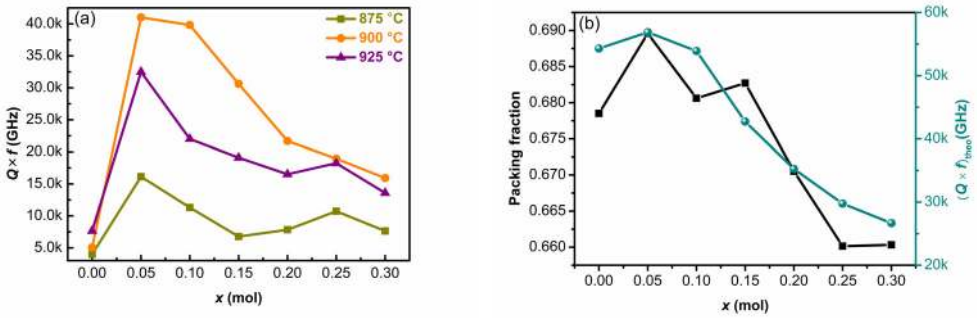

Fig. 7 (a) Quality factor of the $CaMg_{1-x}Li_{2x}Si_2O_6$ (x = 0, 0.05, 0.1, 0.15, 0.2, 0.25, 0.3) samples sintered under different temperatures; (b) the packing fraction and the theoretical quality factor of the $CaMg_{1-x}Li_{2x}Si_2O_6$ (x = 0, 0.05, 0.1, 0.15, 0.2, 0.25, 0.3) samples sintered at 900 ℃.

intrinsic loss and is closely related to lattice vibration. The packing fraction of crystal was determined by the number of formula units per cell unit (Z), V, and the volume of atom in the cell, as described in Eq. (5) [32]:

$$\text{Packing fraction}(\%)=\frac{\text{Volume of atoms in the cell}}{V}\times Z \tag{5}$$

It could be observed that the packing fraction is inversely proportional to V. Figures 3 and 7(a) presented that V and the $Q \times f$ value of the samples sintered at 900 ℃ were in the opposite trend for $0 \leqslant x \leqslant 0.1$ and $0.15 \leqslant x \leqslant 0.3$, whereas $Q \times f$ values varied with the packing fraction combining Figs. 7(a) with 7(b). In particular, the packing fraction depicted in Fig. 7(b) was the sum of the products of the packing fraction of each phase and its volume fraction, implying that packing fraction here took the second phase into account. Therefore, it was explained again that the impact of the second phase on the $Q \times f$ value was high. The $(Q \times f)_{\text{theo}}$ values calculated from the mixture rule [33]:

$$(Q\times f)^{-1}=\sum\frac{V_i'}{(Q\times f)_i} \tag{6}$$

where V_i' and $(Q \times f)_i$ are the volume fraction and $Q \times f$ of each phase, respectively (the $Q \times f$ values of $CaSiO_3$ and Li_2SiO_3 were 25,398 GHz [34] and 9849 GHz [35], respectively), were in the same trend as the measured ones when combining Figs. 7(a) and 7(b). And the measured values were smaller than those of the theoretical ones, confirming the effect of the second phase on the $Q \times f$ value. Moreover, the effect of relative density on $Q \times f$ value could be ignored when $0.05 \leqslant x \leqslant 0.3$. The relative density values of the ceramics sintered at 900 ℃ were above 94%; the highest $Q \times f$ value did not occur at the largest density. Therefore, it could be easily deduced that the intrinsic loss had an equal impact on the $Q \times f$ value to extrinsic loss, and moderate substitution content of Li^+ could decrease the sintering temperature not at the cost of sacrificing the quality factor.

Figure 6(a) presents the variations in dielectric constant with x value at three different sintering temperatures: 875, 900, and 925 ℃. At any sintering temperature in the experiment, the maximum ε_r was obtained at x = 0.1. In general, ε_r is related to relative density, the second phase, and ionic polarizability. Figure 6(b) presents the relationship between ε_r, relative density, and bulk density of samples sintered at 900 ℃. The relative density (ρ) was calculated

through Eq. (7). The theoretical density (ρ_{theo}) was decided via Eq. (8) [16] in the multiphase system.

$$\rho = \frac{\rho_{bulk}}{\rho_{theo}} \tag{7}$$

$$\rho_{theo} = \frac{W_1 + W_2 + W_3 + W_4}{W_1/\rho_1 + W_2/\rho_2 + W_3/\rho_3 + W_4/\rho_4} \tag{8}$$

where ρ_{bulk} represents the bulk density; $\rho_1, \rho_2, \rho_3, \rho_4$, W_1, W_2, W_3, and W_4 represent the theoretical density and weight fraction of $CaMgSi_2O_6$ phase, $CaSiO_3$ phase, Li_2SiO_3 phase, and LBSCA glass, respectively; for LBSCA glass, ρ_4 = 2.36 g/cm^3 [29]. The microwave dielectric constants of $CaMg_{1-x}Li_{2x}Si_2O_6$ samples were consistent with the trends of ρ. Meanwhile, the influence of porosity on ε_r (ε_{rc}) could be obtained according to Eq. (9):

$$\varepsilon_{mea} = \varepsilon_{rc}\left[1 - \frac{3p(\varepsilon_{rc} - 1)}{2\varepsilon_{rc} + 1}\right] \tag{9}$$

where p represents porosity that is opposite to the relative density and ε_{rc} is the dielectric constant corrected by the porosity. The results are listed in Table 2. When combined with the relative density, it was indicated that ε_r was severely affected by ρ and the porosity as Li^+ substitution content increased. Moreover, the observed and theoretical ionic polarizability, α_{obs} and α_{theo}, could be calculated through Clausius–Mosotti equation: Eqs. (10) and (11), which was based on the oxide additivity rule [36], and ionic polarizabilities of cations and oxygen were reported by Shannon [37]. The error between α_{obs} and α_{theo} ($\Delta\alpha$) was calculated by Eq. (12).

$$\alpha_{obs} = \frac{V(\varepsilon_r - 1)}{4b(\varepsilon_r + 2)} \tag{10}$$

$$\alpha_{theo}(CaMg_{1-x}Li_{2x}Si_2O_6) = \alpha_{Ca} + (1-x)\alpha_{Mg} + (2x)\alpha_{Li} + 2\alpha_{Si} + 6\alpha_O \tag{11}$$

$$\Delta\alpha = \left|\frac{\alpha_{obs} - \alpha_{theo}}{\alpha_{theo}} \times 100\%\right| \tag{12}$$

where b is a constant of $4\pi/3$. The calculation results of samples sintered at 900 ℃ are presented in Table 2. In Fig. 6(c), both ε_r and α_{obs} increased first and consequently decreased with x. α_{theo} increased linearly with x, as attributed to the 2 mol Li^+ (1.2 Å^3) substitution for 1 mol Mg^{2+} (1.32 Å^3). The $\Delta\alpha$ is low, as listed in Table 2, facilitating the reliability of the α_{obs}. Besides, α_{obs} was obtained only through the data of $CaMgSi_2O_6$ main phase and it produced consonance well with ε_r, when the weight fraction of the second phase increased with x value. More importantly, combined with the mixture rule:

$$\ln\varepsilon_r = \sum V_i' \ln\varepsilon_{ri} \tag{13}$$

where ε_{ri} represents dielectric constant of each phase (ε_r ($CaSiO_3$) = 6.69 [34], ε_r (Li_2SiO_3) = 7.7 [35]), it could be inferred that ε_r was affected by more ionic polarizability and ρ than the second phase combined with the above analysis.

In general, the τ_f value is determined by the linear expansion coefficient (α_1) and the temperature coefficient of dielectric constant (τ_ε) as presented in Eq. (14).

$$\tau_f = -\left(\alpha_1 + \frac{1}{2}\tau_\varepsilon\right) \tag{14}$$

where α_1 is an empirical constant of approximately 10 ppm/℃. Consequently, τ_f was mainly affected by τ_ε, which was closely related to the oxygen polyhedral distortion (MgO_6 octahedral distortion in $CaMgSi_2O_6$ system). The octahedral distortion (δ) could be calculated via Mg–O bond length, obtained through XRD refinement results, according to Eq. (15). The bond valence, through which the bond strength could be evaluated, V_i of atom i was the sum of all valences v_{ij} from i, calculated via Eqs. (16) and (17) [38].

$$\delta = \frac{1}{6}\sum\left(\frac{R_i - R_A}{R_A}\right) \tag{15}$$

$$V_i = \sum v_{ij} \tag{16}$$

$$v_{ij} = \exp\left(\frac{R_{ij} - d_{ij}}{b}\right) \tag{17}$$

Table 2 ε_{rc}, α_{obs}, α_{theo}, and $\Delta\alpha$ of the $CaMg_{1-x}Li_{2x}Si_2O_6$ (x = 0, 0.05, 0.1, 0.15, 0.2, 0.25, 0.3) samples sintered at 900 ℃

x (mol)	0	0.05	0.1	0.15	0.2	0.25	0.3
ε_{rc}	7.3245	7.5208	7.4895	7.1692	6.8827	6.8982	7.14515
α_{obs}	16.2407	17.9076	18.1070	17.6952	17.7391	17.74181	17.65243
α_{theo}	18.280	18.334	18.388	18.442	18.496	18.550	18.604
$\Delta\alpha$	0.12556	0.02381	0.01551	0.04220	0.04266	0.04555	0.05390

where R_i, R_A, R_{ij}, and d_{ij} represent the bond length, average bond length, bond valence parameter, and the length of a bond between Mg and oxygen in the MgO_6 octahedron, respectively. Besides, b is commonly a constant equal to 0.37 Å, while R_{ij} as 1.661, 1.624, 1.466, and 1.933 Å for Mg–O, Si–O, Li–O, and Ca–O bond, respectively [39,40]. All bond length information and the calculated results are presented in Table 3. As presented in Fig. 8, τ_f and δ of cylinders sintered at 900 ℃ exhibited the same tendency as x value increased, except the porous samples of x = 0, which was due to insufficient sintering. The results well agreed with Lai *et al*. [41,42], which implied that the dependence of τ_f value on δ was high. Besides, the curve of total bond valence (V_{total}) presented in Fig. 8 also corresponded well with the one of τ_f value, which could be explained by the result that higher bond valence results in lower $|\tau_f|$ [43,44]. These phenomena in turn illustrated that although the second phases of $CaSiO_3$ and Li_2SiO_3 were observed, the structural characteristics played an important role in τ_f.

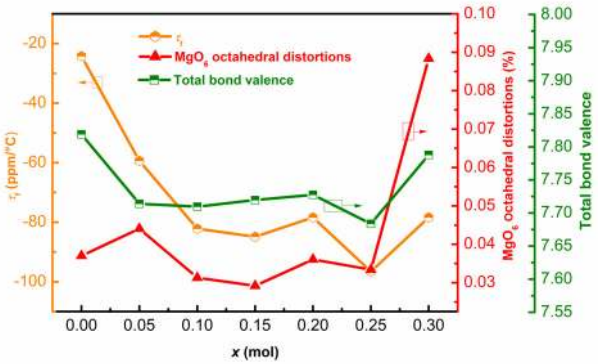

Fig. 8 τ_f, MgO_6 octahedral distortion, and total bond valence of the $CaMg_{1-x}Li_{2x}Si_2O_6$ (x = 0–0.3) samples sintered at 900 ℃.

Table 3 Bond length, MgO_6 octahedral distortion, and total bond valence of the $CaMg_{1-x}Li_{2x}Si_2O_6$ (x = 0, 0.05, 0.1, 0.15, 0.2, 0.25, 0.3) samples sintered at 900 ℃

	Bond type	x (mol)						
		0	0.05	0.1	0.15	0.2	0.25	0.3
Bond length (Å)	Ca1_O1 × 2	2.31047	2.35409	2.34517	2.33304	2.32141	2.35621	2.3735
	Ca1_O2 × 2	2.32076	2.33614	2.33668	2.32433	2.32405	2.34619	2.36359
	Ca1_O3(1) × 2	2.55516	2.54331	2.54059	2.53846	2.51846	2.55902	2.55934
	Ca1_O3(2) × 2	2.75265	2.73447	2.73326	2.70526	2.72712	2.70602	2.75991
	Si1_O1	1.60651	1.61744	1.6289	1.63807	1.64629	1.63474	1.61091
	Si1_O2	1.53561	1.57943	1.57741	1.57922	1.57977	1.56284	1.51783
	Si1_O3(1)	1.71107	1.70073	1.68919	1.68452	1.69012	1.65136	1.67279
	Si1_O3(2)	1.65246	1.66076	1.66353	1.68722	1.68435	1.70171	1.64362
	Mg1_O2 × 2	2.09544	2.04691	2.06264	2.06631	2.04905	2.10107	2.13182
	Mg1_O1(1) × 2	2.06176	2.04468	2.04461	2.03722	2.04421	2.03025	2.02068
	Mg1_O1(2) × 2	2.15943	2.13825	2.13008	2.12265	2.13009	2.11822	2.16782
δ(%)		0.03701	0.044068	0.031303	0.02919	0.03606	0.03340	0.08836
Bond valence	Mg1_O2	0.30907	0.35239	0.33772	0.33439	0.35036	0.30441	0.28013
	Mg1_O1(1)	0.33853	0.35452	0.35459	0.36174	0.35497	0.36862	0.37828
	Mg1_O1(2)	0.25999	0.27530	0.28145	0.28716	0.28144	0.29062	0.25416
	Si1_O1	1.03713	1.00694	0.97623	0.95233	0.93141	0.96094	1.02487
	Si1_O2	1.25618	1.11588	1.12199	1.11651	1.11486	1.16705	1.31802
	Si1_O3(1)	0.78181	0.80397	0.82944	0.83997	0.82736	0.91873	0.86703
	Si1_O3(2)	0.91600	0.89568	0.88900	0.83387	0.84036	0.80184	0.93815
	Ca1_O1	0.36052	0.32043	0.32825	0.33919	0.35002	0.31860	0.30405
	Ca1_O2	0.35063	0.33636	0.33587	0.34727	0.34753	0.32734	0.31231
	Ca1_O3(1)	0.18609	0.19214	0.19356	0.19468	0.20549	0.18416	0.18400
	Ca1_O3(2)	0.10912	0.11461	0.11499	0.12403	0.11691	0.12378	0.10700
	V_{total}	7.81910	7.71407	7.70960	7.71968	7.72752	7.68368	7.78799

4 Conclusions

In this study, the effects of Li^+ substitution for Mg^{2+} on the microwave dielectric properties and microstructure, and the correlation between performance and structure of the $CaMg_{1-x}Li_{2x}Si_2O_6$ ceramics sintered at 875, 900, and 925 ℃ with 0.4 wt% LBSCA as sintering aid, were investigated. The phase compositions detected from the XRD patterns, which were composed of at least two phases ($CaMgSi_2O_6$ and $CaSiO_3$ existed when x varied from 0 to 0.3, and Li_2SiO_3 occurred since x exceeded 0.05), were confirmed by the Rietveld refinement results. SEM micrographs demonstrated that well-uniform morphologies were observed at x = 0.05. The optimal $Q \times f$ value was reached where the fraction of the second phase was the lowest, indicating that the $Q \times f$ value was highly influenced by the second phase, V, and the packing fraction, but the relative density had much less effect on the $Q \times f$ value. The ε_r was not only affected by the relative density, but also was affected by the ionic polarizability, which was closely related to Li^+ ions, and to the second phase. The τ_f values presented nonlinear variations with x and depended highly on the MgO_6 octahedral distortion and the bond valence, despite the existence of the second phase in $CaMg_{1-x}Li_{2x}Si_2O_6$ ceramics. Excellent microwave dielectric properties of $CaMg_{1-x}Li_{2x}Si_2O_6$ ceramics sintered at 900 ℃ were: ε_r = 7.44, $Q \times f$ = 41,017 GHz (f = 15.1638 GHz), and τ_f = −59.3 ppm/℃ when x = 0.05.

Acknowledgements

This study was supported by the National Natural Science Foundation of China (Grant Nos. 61771104 and U1809215).

References

[1] Hsiang HI, Chen CC, Yang SY. Microwave dielectric properties of $Ca_{0.7}Nd_{0.2}TiO_3$ ceramic-filled CaO–B_2O_3–SiO_2 glass for LTCC applications. *J Adv Ceram* 2019, **8**: 345–351.

[2] Weng ZZ, Han ZY, Xiao F, *et al*. Low temperature sintering and microwave dielectric properties of $Zn_{1.8}SiO_{3.8}$ ceramics with $BaCu(B_2O_5)$ additive for LTCC applications. *Ceram Int* 2018, **44**: 14145–14150.

[3] Zhang P, Sun KX, Liu L, *et al*. A novel low loss and low temperature sintering $Li_3(Mg_{1-x}Ca_x)_2NbO_6$ microwave dielectric ceramics by doping LiF additives. *J Alloys Compd* 2018, **765**: 1209–1217.

[4] Li EZ, Yang HC, Yang HY, *et al*. Effects of Li_2O–B_2O_3–SiO_2 glass on the low-temperature sintering of $Zn_{0.15}Nb_{0.3}Ti_{0.55}O_2$ ceramics. *Ceram Int* 2018, **44**: 8072–8080.

[5] Ma XH, Kweon SH, Im M, *et al*. Low-temperature sintering and microwave dielectric properties of B_2O_3-added ZnO-deficient Zn_2GeO_4 ceramics for advanced substrate application. *J Eur Ceram Soc* 2018, **38**: 4682–4688.

[6] Chen HW, Su H, Zhang HW, *et al*. Low-temperature sintering and microwave dielectric properties of $(Zn_{1-x}Co_x)_2SiO_4$ ceramics. *Ceram Int* 2014, **40**: 14655–14659.

[7] Song XQ, Du K, Li J, *et al*. Low-fired fluoride microwave dielectric ceramics with low dielectric loss. *Ceram Int* 2019, **45**: 279–286.

[8] Cheng K, Li CC, Xiang HC, *et al*. $LiYGeO_4$: Novel low-permittivity microwave dielectric ceramics with intrinsic low sintering temperature. *Mater Lett* 2018, **228**: 96–99.

[9] Cheng K, Tang Y, Xiang HC, *et al*. Two novel low permittivity microwave dielectric ceramics Li_2TiMO_5 (M = Ge, Si) with abnormally positive τf. *J Eur Ceram Soc* 2019, **39**: 2680–2684.

[10] Fang WS, Cheng K, Xiang HC, *et al*. Phase composition and microwave dielectric properties of low permittivity AGeO3 (A = Mg, Zn) ceramics. *J Alloys Compd* 2019, **799**: 495–500.

[11] Li CC, Xiang HC, Xu MY, *et al*. Li_2AGeO_4 (A = Zn, Mg): Two novel low-permittivity microwave dielectric ceramics with olivine structure. *J Eur Ceram Soc* 2018, **38**: 1524–1528.

[12] Liu B, Hu CC, Huang YH, *et al*. Crystal structure, infrared reflectivity spectra and microwave dielectric properties of $CaAl_2O_4$ ceramics with low permittivity. *J Alloys Compd* 2019, **791**: 1033–1037.

[13] Song XQ, Du K, Li J, *et al*. Crystal structures and microwave dielectric properties of novel low-permittivity $Ba_{1-x}Sr_xZnSi_3O_8$ ceramics. *Mater Res Bull* 2019, **112**: 178–181.

[14] Yin CZ, Li CC, Yang GJ, *et al*. $NaCa_4V_5O_{17}$: A low-firing microwave dielectric ceramic with low permittivity and chemical compatibility with silver for LTCC applications. *J Eur Ceram Soc* 2020, **40**: 386–390.

[15] Li CC, Yin CZ, Chen JQ, *et al*. Crystal structure and dielectric properties of germanate melilites $Ba_2MGe_2O_7$ (M = Mg and Zn) with low permittivity. *J Eur Ceram Soc* 2018, **38**: 5246–5251.

[16] Qin TY, Zhong CW, Qin Y, *et al*. Low-temperature sintering mechanism and microwave dielectric properties of $ZnAl_2O_4$-LMZBS composites. *J Alloys Compd* 2019, **797**: 744–753.

[17] Song XQ, Lu WZ, Wang XC, *et al*. Sintering behaviour and microwave dielectric properties of $BaAl_{2-2x}(ZnSi)_xSi_2O_8$ ceramics. *J Eur Ceram Soc* 2018, **38**: 1529–1534.

[18] Sun HP, Zhang QL, Yang H, *et al*. $(Ca_{1-x}Mg_x)SiO_3$: A low-permittivity microwave dielectric ceramic system. *Mater Sci Eng: B* 2007, **138**: 46–50.

[19] Li H, Chen XQ, Zhang PC, *et al*. Influence of Mn^{2+} introduction on microwave dielectric properties of

$CaMgSi_2O_6$ ceramic. *Ceram Int* 2019, **45**: 24425–24430.

[20] Tang B, Xiang QY, Fang ZX, *et al*. Influence of Cr^{3+} substitution for Mg^{2+} on the crystal structure and microwave dielectric properties of $CaMg_{1-x}Cr_{2x}/3Si_2O_6$ ceramics. *Ceram Int* 2019, **45**: 11484–11490.

[21] Lai YM, Su H, Wang G, *et al*. Improved microwave dielectric properties of $CaMgSi_2O_6$ ceramics through CuO doping. *J Alloys Compd* 2019, **772**: 40–48.

[22] Wang HP, Li DH, Yang QH, *et al*. Sintering behavior and microwave dielectric properties of $CaMgSi_2O_6$ ceramics with Al_2O_3 addition. *Mater Res Bull* 2014, **54**: 66–72.

[23] Wang HP, Xu SQ, Zhai SY, *et al*. Effect of B_2O_3 additives on the sintering and dielectric behaviors of $CaMgSi_2O_6$ ceramics. *J Mater Sci Technol* 2010, **26**: 351–354.

[24] Joseph T, Sebastian MT, Sreemoolanadhan H, *et al*. Effect of glass addition on the microwave dielectric properties of $CaMgSi_2O_6$ ceramics. *Int J Appl Ceram Technol* 2009, **7**: E98–E106.

[25] Chang SY, Pai HF, Tseng CF, *et al*. Microwave dielectric properties of ultra-low temperature fired Li_3BO_3 ceramics. *J Alloys Compd* 2017, **698**: 814–818.

[26] Thomas D, Sebastian MT. Temperature-compensated $LiMgPO_4$: A new glass-free low-temperature cofired ceramic. *J Am Ceram Soc* 2010, **93**: 3828–3831

[27] Zhou D, Randall CA, Pang LX, *et al*. Microwave dielectric properties of Li_2WO_4 ceramic with ultra-low sintering temperature. *J Am Ceram Soc* 2011, **94**: 348–350.

[28] Du XY, Su H, Zhang HW, *et al*. Effects of Li-ion substitution on the microwave dielectric properties of low-temperature sintered ceramics with nominal composition $Li_{2x}Mg_{2-x}SiO_4$. *Ceram Int* 2018, **44**: 2300–2303.

[29] Jing XL, Tang XL, Tang WH, *et al*. Effects of Zn^{2+} substitution on the sintering behaviour and dielectric properties of $Li_2Mg_{1-x}Zn_xSiO_4$ ceramics. *Appl Phys A* 2019, **125**: 415.

[30] Fan YZ, Zhou ZY, Liang RH, *et al*. The effect of A-site nonstoichiometry on the microstructure, electric properties, and phase stability of $NaNbO_3$ polycrystalline ceramics. *J Eur Ceram Soc* 2019, **39**: 4712–4718.

[31] Li EZ, Yang X, Yang HC, *et al*. Crystal structure, microwave dielectric properties and low temperature sintering of $(Al_{0.5}Nb_{0.5})^{4+}$ co-substitution for Ti^{4+} of $LiNb_{0.6}Ti_{0.5}O_3$ ceramics. *Ceram Int* 2019, **45**: 5418–5424.

[32] Kim ES, Chun BS, Freer R, *et al.* Effects of packing fraction and bond valence on microwave dielectric properties of $A^{2+}B^{6+}O_4$ (A^{2+}:Ca,Pb,Ba; B^{6+}:Mo,W) ceramics. *J Eur Ceram Soc* 2010, **30**: 1731–1736.

[33] Wu MJ, Zhang YC, Xiang MQ. Synthesis, characterization and dielectric properties of a noveltemperature stable $(1-x)CoTiNb_2O_{8-x}ZnNb_2O_6$ ceramic. *J Adv Ceram* 2019, **8**: 228–237.

[34] Ouyang LH, Wang WQ, Fan HC, *et al.* Sintering behavior and microwave performance of $CaSiO_3$ ceramics doped with $BaCu(B_2O_5)$ for LTCC applications. *Ceram Int* 2019, **45**: 18937–18942.

[35] Lai YM, Tang XL, Zhang HW, *et al.* Relationship between the structure and microwave dielectric properties of non-stoichiometric $Li_{2+x}SiO_3$ ceramics. *Ceram Int* 2017, **43**: 2664–2669.

[36] Shannon RD, Rossman GR. Dielectric constant of $MgAl_2O_4$ spinel and the oxide additivity rule. *J Phys Chem Solids* 1991, **52**: 1055–1059.

[37] Shannon RD. Dielectric polarizabilities of ions in oxides and fluorides. *J Appl Phys* 1993, **73**: 348–366.

[38] Cheng K, Li CC, Yin CZ, *et al*. Effects of Sr^{2+} substitution on the crystal structure, Raman spectra, bond valence and microwave dielectric properties of $Ba_{3-x}Sr_x(VO4)_2$ solid solutions. *J Eur Ceram Soc* 2019, **39**: 3738–3743.

[39] Yee TA, Suescun L, Rabuffetti FA. Bond valence parameters for alkali- and alkaline-earth-oxygen pairs: Derivation and application to metal−organic compounds. *J Solid State Chem* 2019, **270**: 242–246.

[40] Brese NE, O'Keeffe M. Bond-valence parameters for solids. *Acta Crystallogr Sect B* 1991, **47**: 192–197

[41] Lai YM, Tang XL, Huang X, *et al*. Phase composition, crystal structure and microwave dielectric properties of $Mg_{2-x}Cu_xSiO_4$ ceramics. *J Eur Ceram Soc* 2018, **38**: 1508–1516.

[42] Lai YM, Su H, Wang G, *et al*. Low-temperature sintering of microwave ceramics with high *Qf* values through LiF addition. *J Am Ceram Soc* 2019, **102**: 1893–1903

[43] Xia WS, Li LX, Ji LJ, *et al.* Phase evolution, bond valence and microwave characterization of $(Zn_{1-x}Ni_x)Ta_2O_6$ ceramics. *Mater Lett* 2012, **66**: 296–298.

[44] Park HS, Yoon KH, Kim ES. Effect of bond valence on microwave dielectric properties of complex perovskite ceramics. *Mater Chem Phys* 2003, **79**: 181–183.